

# Thermo-physical properties of plasma electrolytic oxide coatings on aluminium

J.A. Curran, T.W. Clyne\*

*Department of Materials Science and Metallurgy, Cambridge University, Pembroke Street, Cambridge CB2 3QZ, UK*

Available online 26 February 2005

## Abstract

Plasma electrolytic oxide coatings appear to offer attractive combinations of hardness, wear resistance, corrosion resistance and interfacial adhesion. In order to optimise such characteristics, however, more basic thermo-physical property data are required, together with an understanding of how they are affected by processing conditions and microstructure. In the present study, coatings were produced on 6082 aluminium and characterised using profilometry, scanning electron microscopy, X-ray diffraction and nanoindentation. The in-plane thermal expansivity of detached coatings was measured by dilatometry to be about 8 microstrain  $K^{-1}$ . There is thus a rather substantial mismatch between the expansivities of coating and substrate, amounting to about 15 microstrain  $K^{-1}$ . The global in-plane Young's modulus was estimated using cantilever bending of sandwich coated substrates and also by measuring the curvature generated in a bi-material beam on cooling to low temperature. It was found to lie in the approximate range of 10–40 GPa. Values of this order, which are low compared with the figure of around 370 GPa expected for fully dense polycrystalline alumina, are thought to be associated with the presence of a network of microcracks and voids. A low value is expected to be beneficial in terms of conferring good strain tolerance, and hence resistance to spallation driven by differential thermal expansion.

© 2005 Elsevier B.V. All rights reserved.

*Keywords:* Plasma electrolytic oxidation; Alumina coatings; Discharge channels; Microarc oxidation

## 1. Introduction

There are increasing levels of interest in plasma electrolytic oxide (PEO) coatings. They can be quickly and economically produced on components with almost any shape and size, made of various metals, and the thickness range is substantial [1]. Furthermore, it appears that these coatings can exhibit low porosity levels and excellent interfacial adhesion [2,3]. They are being explored for various applications, including those for which wear resistance [4–8], corrosion resistance [6,8,9] and thermal protection [10,11] are being sought.

However, much remains to be established before these coatings can be efficiently exploited and find widespread use. In particular, despite extensive study of the deposition process [12–15] and of coating microstructures [16–18],

relatively little is currently known about the thermo-physical properties of PEO coatings, or how these relate to either microstructure or processing conditions. Such properties are clearly important. For example, concern has already been expressed about differential thermal expansion misfit strains and stresses [1,3], but these cannot be investigated properly without a knowledge of the elastic constants and thermal expansivity of the coating, and the residual stresses introduced during production.

In the present study, coating microstructures have been examined using X-ray diffraction, optical microscopy and scanning electron microscopy. Optical interferometry and nanoindentation have been used to characterise the surface roughness, porosity, hardness and local stiffness. Finally, cantilever beam bending, dilatometry and curvature measurements after cooling of bi-material beams have been used to evaluate global elastic constants and thermal expansivities. An attempt is made to establish correlations between these properties and microstructural features.

\* Corresponding author.

*E-mail address:* [twc10@cam.ac.uk](mailto:twc10@cam.ac.uk) (T.W. Clyne).

## 2. Experimental procedures

### 2.1. Sample preparation

Coatings were generated on square coupons (50×50×4 mm) of aluminium alloy BS Al-6082, using the Keronite™ process. AC power was applied with a 50 Hz modulation. The voltage was in the 400–600 V RMS range in the anodic half-cycle and 150–250 V RMS in the cathodic half-cycle, controlled so as to maintain a constant current density (of approximately 1 kA m<sup>-2</sup>). The electrolyte consisted of an aqueous solution of tetra-sodium pyrophosphate (3–5 g l<sup>-1</sup>), sodium silicate solution (specific gravity 1.5, 3–5 g l<sup>-1</sup>), and potassium hydroxide (1–2 g l<sup>-1</sup>). Treatment times were selected to give coating thicknesses of approximately 5, 10, 40, 60, 80 and 100 μm based on an approximate growth rate of 1 μm/min. Thicknesses were measured using an Oxford Instruments CMI 100 thickness gauge, which uses eddy currents induced in the substrate to measure coating thickness with an accuracy of 1 μm. The accuracy of this technique was verified by microscopy of polished sections. Coated specimens were sectioned, using a low-speed rotating diamond saw, hot-mounted in resin, ground, using SiC papers, and polished using diamond paste and colloidal silica. For some purposes, coatings were detached from the substrate. This was done by immersion in a warm, saturated solution of NaOH for 1–2 min.

### 2.2. Microstructural studies

SEM observations were made using a JEOL 5500 microscope. Some observations were made in low vacuum mode, while others were made in high vacuum on specimens sputter-coated with platinum (to minimise surface charging). Topographic studies were carried out, using a Wyko RS-2 interferometric profilometer, on untreated coating surfaces, in order to measure the surface roughness and explore surface features. A Phillips PW 1710 X-ray diffractometer was used to perform θ–2θ scans from 10° to 120° with a 0.02° step size. A CuK<sub>α</sub> radiation source was used, with a 40 kV accelerating voltage and a 40 mA filament current. Data were obtained from as-deposited free surfaces. Serial dry grinding of the coating surface was then used to collect data at nominal depths through the thickness of the coating. Phase proportions were determined by Rietveld analysis [19], together with profile fitting of the low-angle amorphous peaks.

### 2.3. Thermo-physical property measurement

The thermal expansion behaviour of detached coatings was investigated using a Netszch 402L push-rod dilatometer, over the temperature range 20–700 °C. This allowed evaluation of the (in-plane) thermal expansivity, which was found to be approximately constant over this temperature range.

The global in-plane Young's modulus of coatings was measured using two techniques. Firstly, cantilever bending experiments were carried out on sandwich bi-material beams, consisting of relatively thick (100 μm) PEO coatings on both sides of relatively thin (~400 μm) substrates. Loads were applied incrementally (by adding ball bearings to a small receptacle suspended from the beam) and displacements were measured using a scanning laser extensometer. Elastic behaviour was confirmed by checking that load-deflection plots were linear and reversible. The following standard expression gives the deflection, δy, exhibited by such a beam, at a distance x along its length, when subjected to a load P at a distance L along its length.

$$\delta y = \frac{Px^2}{6(E_s I_s + E_c I_c)} (3L - x) \quad (1)$$

where  $E_c$ ,  $E_s$  are the Young's moduli of coating and substrate, respectively, and the corresponding moments of inertia (about the neutral axis at the mid-plane) are given by

$$I_s = \frac{bh^3}{12} \text{ and } I_c = \frac{b}{12} (d^3 - h^3) \quad (2)$$

in which  $b$  is the beam width,  $d$  is the total beam thickness and  $h$  is the thickness of the substrate.

Secondly, stiffness values were also obtained via measurement of the specimen curvature,  $\kappa$ , induced by immersing asymmetrical bi-material beams (substrates coated on one side only) in liquid nitrogen, using the following relationship [20]:

$$\kappa = \frac{6E_c E_s (t_c + t_s) t_c t_s (\alpha_c - \alpha_s) \Delta T}{E_c^2 t_c^4 + 4E_c E_s t_c^3 t_s + 6E_c E_s t_c^2 t_s^2 + 4E_c E_s t_c t_s^3 + E_s^2 t_s^4} \quad (3)$$

where  $\Delta T$  is the temperature change,  $t_c$ ,  $t_s$  are the thicknesses and  $\alpha_c$ ,  $\alpha_s$  are the thermal expansivities of coating and substrate, respectively. The curvature, which is uniform along its length, was established from displacement measurements (made with a scanning laser beam device), using the geometrical relationship

$$\kappa = \frac{2}{\sqrt{(x^2 + \delta y^2)}} \sin \left[ \tan^{-1} \left( \frac{\delta y}{x} \right) \right] \quad (4)$$

in which  $\delta y$  is the lateral displacement at a distance  $x$  along the length of the specimen. The Young's modulus of the coating was obtained from Eq. (3), after substituting the experimentally measured curvature value. This process was repeated for several similar specimens. The expansivity values obtained for coating and substrate, using the dilatometer, were employed in the calculation.

### 2.4. Nanoindentation

Nanoindentation was performed on polished cross-sections and in-plane sections, using a Micromaterials

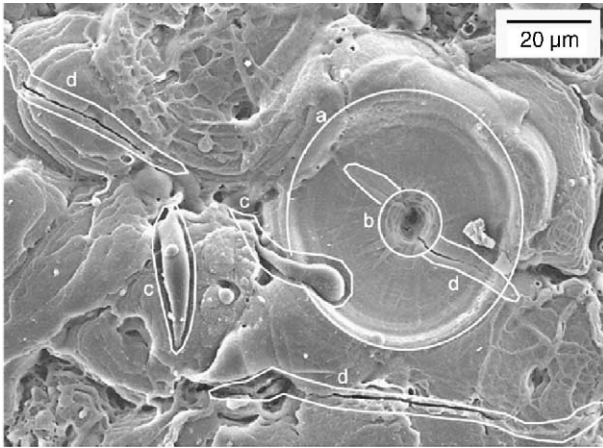


Fig. 1. SEM micrograph of the free surface of a 40  $\mu\text{m}$  thick coating, showing typical features of a PEO coating surface. These include (a) a re-solidified pool or crater, (b) the central sink-hole ("pipe") in such a pool, (c) material ejected from such pools and (d) localised microcracking.

Nanotest 600 machine. A Berkovitch indenter was used with loads of 10 mN and 50 mN. Hardness was calculated from load and indentation depth data, while the local stiffness was determined from the unloading response, using the standard Oliver and Pharr technique [21]. It may be noted that this stiffness differs from that measured by beam bending and bi-material curvature measurements in that: (a) it is local, and hence influenced by defects such as porosity only if the indenter happens to probe a region containing such a defect and (b) it is obtained under predominantly compressive loading.

### 3. Coating microstructure and morphology

#### 3.1. Surface topography

The surfaces of PEO coatings exhibit several features indicative of the physical phenomena occurring during growth. An example is shown in Fig. 1. Repeated volcano-like eruptions appear to occur, which are a consequence of discrete localised discharge events. These lead to the formation of craters, with deep central shrinkage holes or pipes. There are also numerous microcracks, many of them radially oriented, as might be expected during solidification of a melt pool in a brittle material. Furthermore, irregularly shaped regions can be seen around these pools, with the appearance of having been ejected from them as liquid globules.

On studying such free surfaces on coatings of variable thickness, some clear trends become apparent (Fig. 2). For example, it can be seen that the areal density of discharge craters drops off as the thickness increases. It is also noticeable that the surface roughness rises as the coating thickness increases, presumably reflecting the increasing energy and violence of individual discharges. This is consistent with the energy associated with individual discharges increasing as the coating thickness goes up, with the overall power level being held constant. More substantial craters and pipes would thus be expected, and a higher incidence of ejecta, leading to increased surface roughness. These characteristics are quantified in Fig. 3, which shows plots of the crater population density and the surface roughness as a function of coating thickness.

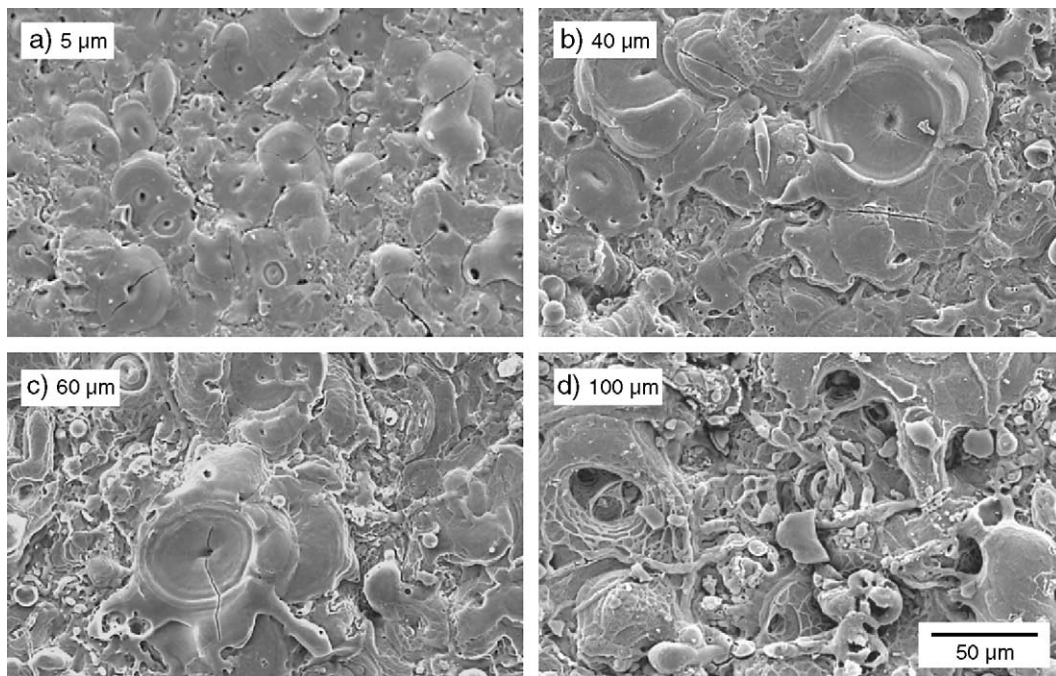


Fig. 2. SEM micrographs showing free surfaces of coatings with different thicknesses, revealing trends in surface topography.

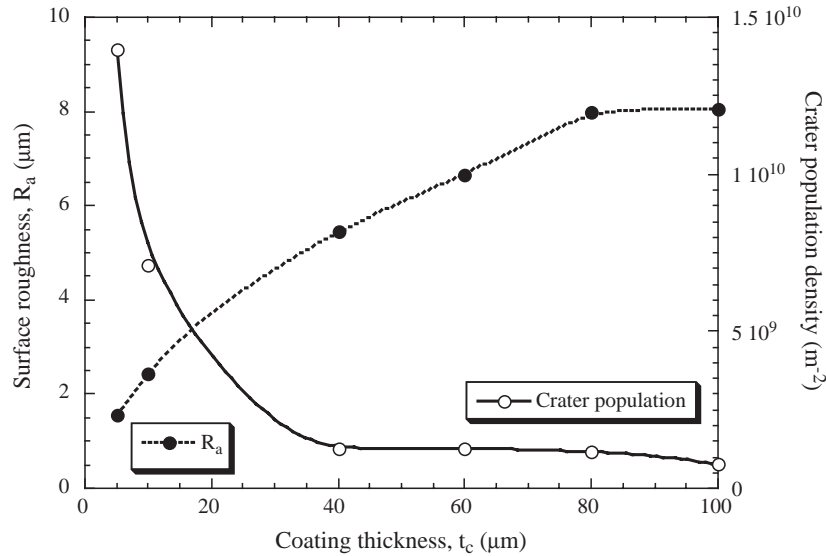


Fig. 3. The surface roughness and areal density of visible craters on the free surface (measured by image analysis), as a function of coating thickness.

It appears that the process is approaching a limit for stable coating growth, which, for this particular alloy/electrolyte combination and power profile, is known to be about 100  $\mu\text{m}$ . As this limit is approached, the discharges begin to localise. Typical reported growth rates [7,14] are constant (at about 1  $\mu\text{m}/\text{min}$  for normal coating growth on aluminium). However, it is widely recognised that there is an upper limit on the achievable thickness, although its value may vary between different systems. This suggests that there is a regime of stable coating growth where although growth (discharge) events become fewer and more energetic as thickness rises, the average growth rate does remain approximately constant. However, a thickness is eventually reached at which discharge events become localised at specific defects, at which point further stable growth is effectively impossible.

Fig. 4(a) shows a micrograph of the underside of a detached 100  $\mu\text{m}$  coating. This exhibits globular features approximately 10  $\mu\text{m}$  in diameter, with a similar areal population density to that of the crater cores on the outer surface. (Some large precipitates are also apparent in this image, which were formed during dissolution of the substrate.) This suggests that the discharges penetrate through the entire thickness of the coating. This is confirmed by Fig. 4(b), which is a higher magnification image of a region where the thin oxide crust had been damaged in the de-bonding process, showing a channel which appears to penetrate through the complete thickness of the coating. From both micrographs, it would seem that the detaching process has little, if any, effect on the overall integrity of the coating.

### 3.2. Through-thickness microstructure

Fig. 5 shows a backscattered SEM micrograph of a polished cross-section of a coating. Even at this low

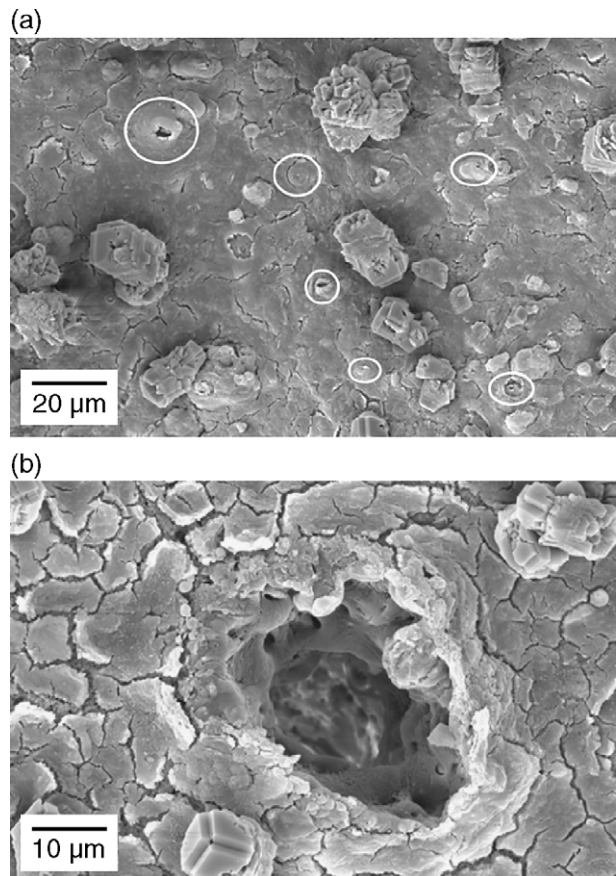


Fig. 4. SEM micrographs of the underside of a detached 100  $\mu\text{m}$  coating, showing (a) a low magnification view, with circles drawn around globular features corresponding to through-thickness discharge channels, and (b) a high magnification image of such a channel, showing a pore which appears to penetrate the entire thickness of the coating.

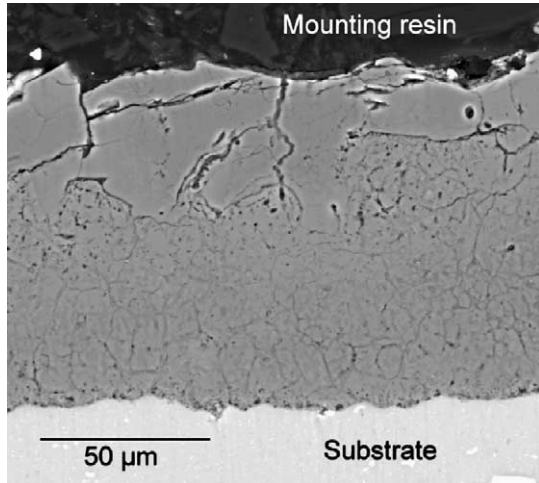


Fig. 5. Back-scattered SEM micrograph of a polished cross-section through a 100  $\mu\text{m}$  thick coating, showing surface cracks, shrinkage pipes and an extensive network of micro-defects.

magnification, and recognising the possibility of the polishing process generating some artefacts, it can be seen that these coatings contain a fairly dense network of shrinkage pipes and microcracks. While it would not be expected that any single discharge channel would lie within the sectioned plane throughout its length, some such channels can be seen in the image, since backscattered mode allows a degree of sub-surface imaging. It can be seen that some channels do appear to penetrate the entire thickness of the coating. This cross-section also reveals two distinct structural layers. There is an inner region, with a dense network of small channels and microcracks, which is presumably the product of the many previous discharges during coating growth. The outer region, marked only with the most recent discharges, appears to have been subjected to an annealing treatment of

some sort, perhaps by heating from more energetic surface discharges. Such an effect has been suggested by Yerokhin et al. [13].

### 3.3. Phase constitution

Fig. 6 is a typical X-ray diffraction  $\theta$ - $2\theta$  trace for the coatings under consideration. It has been fully indexed and is shown to consist of  $\alpha$ - $\text{Al}_2\text{O}_3$  and  $\gamma$ - $\text{Al}_2\text{O}_3$ . There is also a substantial fraction of amorphous material, indicated by the broad background peaks at approximately  $30^\circ$  and  $60^\circ$ . Finally, there appears to be a significant amount of textured aluminium, but this is probably due to X-ray penetration through to the aluminium substrate.

Fig. 7 shows the results of phase analysis by Rietveld refinement, together with the serial grinding of the surface of a 100- $\mu\text{m}$  thick coating. It is presented in the form of a plot of the phase proportion as a function of nominal depth below the free surface. It should be noted that there is an inherent error in the nominal depth since the depth probed by each scan is finite and increases with angle of incidence. The presence of amorphous material also makes penetration harder to quantify. As noted earlier, it is likely that the measured proportion of “aluminium” is merely a consequence of X-ray penetration through to the substrate and thus provides an indication of the error in this method. In particular, the rapid increase in aluminium proportion beyond a nominal depth of 70  $\mu\text{m}$  is indicative of the substrate being probed. Even taking into account this uncertainty, there are significant trends in the data. These trends are confirmed by a simpler analysis based on the relative integrated intensities of the  $(113)_\alpha$  and  $(400)_\gamma$  peaks alone.

The proportion of amorphous material remains constant at about 30% throughout the thickness. However, while the

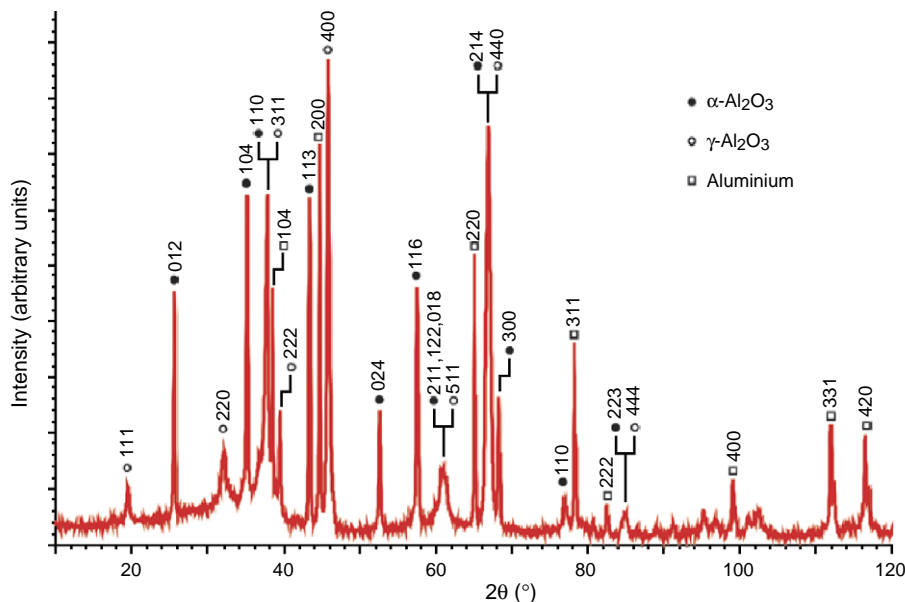


Fig. 6. Indexed  $\theta$ - $2\theta$  X-ray diffraction pattern for the surface of a 100  $\mu\text{m}$  coating after polishing away the outer 40  $\mu\text{m}$ .

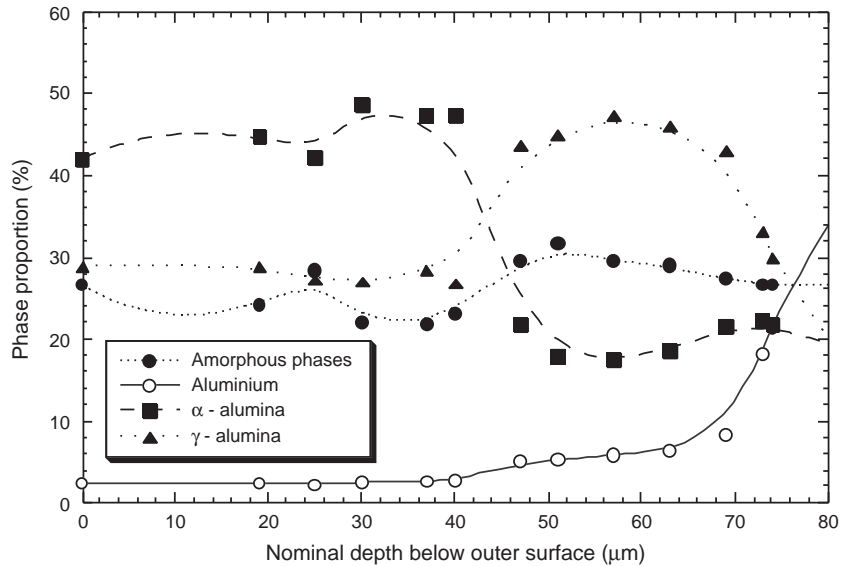


Fig. 7. X-ray diffraction data in the form of a plot of the phase proportions against the nominal depth below the free surface for surface scans during the progressive polishing of a 100  $\mu\text{m}$  thick coating.

remaining material is predominantly composed of the more stable  $\alpha\text{-Al}_2\text{O}_3$  phase in the outer 40  $\mu\text{m}$  or so, there is then a switch to the metastable  $\gamma\text{-Al}_2\text{O}_3$  phase becoming predominant over the next 30  $\mu\text{m}$ .

These phase profiles bear little resemblance to those previously reported [15,22]. However, they are at least consistent with the observation that there is an outer layer, 30–40  $\mu\text{m}$  thick, with a noticeably different microstructural appearance—see Fig. 5. Moreover, the appearance of this outer layer does suggest that it has effectively been subjected to a series of high temperature annealing treatments, of short duration, but distinguishable from rapid quenching. This might be expected to yield a high proportion of the stable  $\alpha\text{-Al}_2\text{O}_3$  phase. It is also significant that a high proportion of amorphous material is detected. Rapid quenching is expected to favour the formation of amorphous phases and  $\gamma\text{-Al}_2\text{O}_3$ . It would appear that the  $\gamma\text{-Al}_2\text{O}_3$  can be converted to  $\alpha\text{-Al}_2\text{O}_3$  by the heat treatment to which the outer layers are effectively subjected during the violent discharge events, whereas the amorphous material does not transform so readily. It is also possible that the distinct layers are a consequence of different modes of growth within and outside the original aluminium substrate. However, it is clear that further work is needed in order to confirm any of these suggestions.

## 4. Physical properties

### 4.1. Thermal expansivity

Approximately linear plots were obtained of length change against temperature. The gradients all indicated an in-plane thermal expansivity for the coatings of about  $8.2 \pm 0.1$  microstrain  $\text{K}^{-1}$ . This was not dependent on

coating thickness. The value is actually fairly typical of handbook data for alumina and it is unsurprising that little deviation is observed, since expansivity is not expected to be sensitive to the presence of defects such as microcracks and porosity.

However, it is certainly worth noting that the value is appreciably smaller than the figure of about 23 microstrain  $\text{K}^{-1}$  typically expected for aluminium and its alloys. A moderate temperature change of, say, 200 K would thus be expected to generate a misfit strain of about 3 millistrain. Assuming a massive substrate, and a coating stiffness of 370 GPa (typical of dense alumina), this would lead to in-plane stresses within the coating having a magnitude of about 1 GPa, which would in turn generate a large driving force for debonding ( $\sim 150 \text{ J m}^{-2}$  for a 100  $\mu\text{m}$  thick coating). These figures suggest that the danger of spallation during temperature excursions might be substantial.

### 4.2. Global Young's modulus

Plots are shown in Fig. 8 of Young's modulus values deduced for the coatings, using (a) bending of a sandwich cantilever beam (substrate coated on both sides) and (b) cooling of a bi-material beam (substrate coated on one side only). These plots show the range of measured data and the corresponding deductions of Young's modulus. On each plot, a curve showing the dependence of Young's modulus on the measured parameter for a specific case is included to give some indication of the significance of results.

It can be seen that, while there is some scatter in the data, and the values obtained using the two different approaches are not in close agreement, the experimentally measured in-plane stiffness is relatively low, compared with the figure expected for dense alumina ( $\sim 370$  GPa). The cantilever bending data suggest a value of around 10 GPa, while the

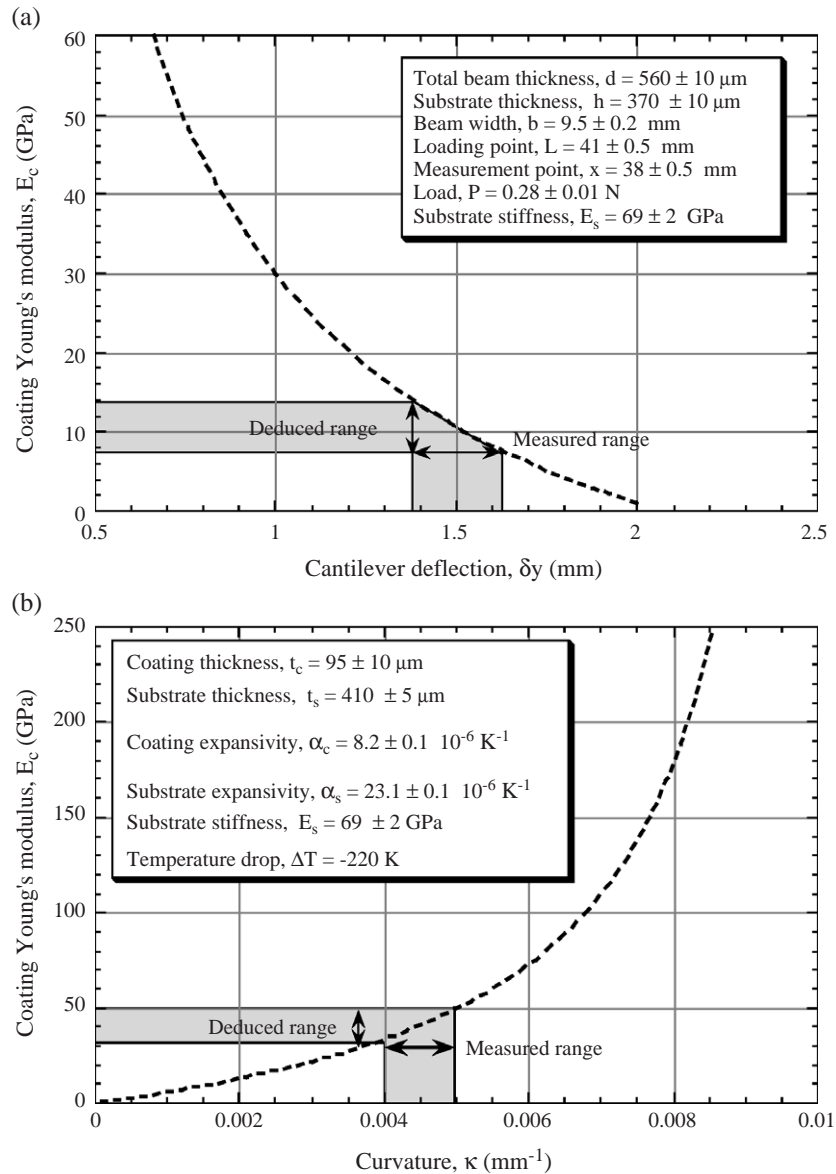


Fig. 8. Global Young's modulus data for the coatings. Plots are shown of the dependence of Young's modulus on (a) observed cantilever deflection and (b) observed bi-material beam curvature (according to Eq. (1)) for specific cases, while the ranges of experimentally obtained data and of deduced Young's modulus are marked on the plots.

bi-material beam cooling experiments indicate a figure of around 40 GPa. The discrepancy between these two figures looks a little large, but it is worth noting that the cooling experiments put the coating into compression, which may raise its apparent stiffness as the microcracks etc become closed. During the sandwich beam bending, on the other hand, the average of tensile and compressive moduli is being measured. In any event, the main conclusion is that the global in-plane stiffness is about an order of magnitude lower than that expected for dense alumina. This is not really surprising when account is taken of the network of micro-cracks and micro-pores present in the coatings. It may also be noted that beneficial effects are expected to arise from having a relatively low value. For example, if the

coating stiffness is 30 GPa, then the calculations outlined in the previous section become altered such that the inplane stress level in the coating is reduced to about 100 MPa and the corresponding strain energy release rate falls to about  $15 \text{ J m}^{-2}$ . These relatively low values are at least consistent with the observation that even relatively thick coatings do not appear to be severely prone to debonding during either heating or cooling.

#### 4.3. Hardness and local Young's modulus

Data are shown in Fig. 9 for the local hardness and stiffness, obtained using nanoindentation on a polished transverse section from a  $80 \mu\text{m}$  thick coating, as a function

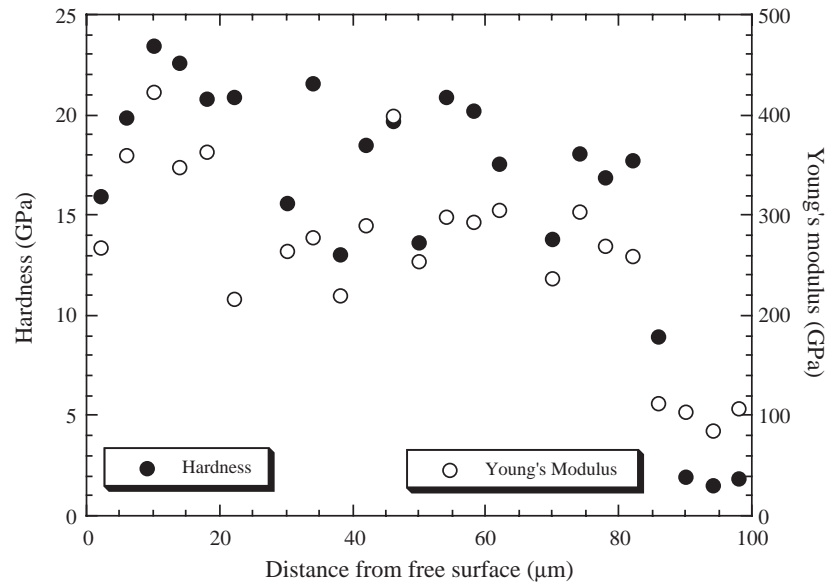


Fig. 9. Profiles of hardness and local Young's modulus through the thickness of a 80  $\mu\text{m}$  thick coating, as measured by nanoindentation using a 10 mN load and a Berkovitch indenter.

of depth below the surface. While there is clearly a lot of scatter in the data, associated with the possibility that the indent could be close to a pore or other microstructural defect, it can be seen that there is a tendency for the hardness to be higher near the free surface, where there is a high proportion of  $\alpha\text{-Al}_2\text{O}_3$ —see Fig. 7. Furthermore, the hardness in this region reaches about 23 GPa, which is comparable to that expected for sintered  $\alpha\text{-Al}_2\text{O}_3$  (measured as 21 GPa using the same instrument).

The Young's modulus plots follow a similar trend, with a slightly higher average value near the free surface, but again a lot of scatter. It is certainly noticeable that the values obtained are of the same order as is expected for dense alumina and hence are much higher than the global values reported in the previous section. This is broadly as expected, since the procedure is sensing the local stiffness and will thus be little affected in most cases by porosity or cracks. Furthermore, the material is being loaded predominantly in compression, which also makes it less likely that very low values would be obtained as a consequence of the presence of cracks, etc.

## 5. Summary

The following conclusions can be drawn from this work, relating to PEO coatings on aluminium-based substrates.

- (i) The coatings form via a series of electrical discharge events, which create columnar melt pools extending through the thickness of the coating and cause some eruption of molten material at the free surface.
- (ii) These discharge events become more energetic and less frequent as the coating thickness increases. For

the conditions employed in the present study, their population density started at about  $1.5 \times 10^{10} \text{ m}^{-2}$  (spacing  $\sim 8 \mu\text{m}$ ), but fell to about  $1 \times 10^9 \text{ m}^{-2}$  (spacing  $\sim 30 \mu\text{m}$ ) as the coating thickness rose to about 100  $\mu\text{m}$ . The surface roughness increased during this process, from  $\sim 2 \mu\text{m}$  to  $\sim 8 \mu\text{m}$   $R_a$ . As the discharge events become more localised and more violent, further stable growth becomes difficult, imposing an upper limit on the coating thickness.

- (iii) The process generates a network of fine cracks, pipes and pores within the coating.
- (iv) The coatings contain about 30% of amorphous material throughout the thickness. The remaining material is predominantly  $\alpha\text{-Al}_2\text{O}_3$  near the free surface, but contains more of the metastable  $\gamma\text{-Al}_2\text{O}_3$  phase near the substrate. Furthermore, the microstructure is coarser near the free surface, to such an extent that the coating exhibits a noticeable two-layer appearance. These differences are provisionally attributed to the near-surface regions having been subjected to an annealing-type process, as a consequence of the relatively large heat-affected zones around the energetic discharge events which occur as the coating becomes relatively thick.
- (v) The thermal expansivity of the coatings has been measured to be about  $8 \text{ microstrain K}^{-1}$ . This is similar to previously reported values for dense alumina. This property is not expected to exhibit much sensitivity to the phase constitution or microstructure.
- (vi) The global in-plane stiffness of the coatings has been found to be relatively low. Cantilever bending experiments on coating/substrate composite beams suggested a figure around 10 GPa, while a procedure involving curvature measurement on cooling of

coated substrates, which involved putting the coating into compression, suggested a figure closer to 40 GPa. The difference between these figures and a typical value for dense alumina of 370 GPa is attributed to the effect of the network of cracks and fine pores.

- (vii) Nanoindentation was used to measure the hardness and the local stiffness. Coating hardness (~20 GPa) and stiffness (~300 GPa) were both found to be similar to those of dense alumina. This is consistent with the fact that these experiments sense the local properties and are not in most cases strongly affected by defects such as cracking or porosity.

### Acknowledgements

Funding for this work has come from EPSRC, in the form of an Industrial CASE award sponsored by DSTL. The authors are grateful for the ongoing involvement and support of Prof. Richard Jones, of DSTL. There has also been extensive collaboration with Dr. Pavel Shashkov, of Keronite plc, who has provided all of the samples examined in this investigation. Finally, the help of Mr. Ulrich Pennig, of Göttingen University, with some of the XRD measurements, is gratefully acknowledged.

### References

- [1] A.L. Yerokhin, et al., *Surf. Coat. Technol.* 122 (2–3) (1999) 73.
- [2] X. Nie, et al., *Surf. Coat. Technol.* 119 (1999) 1055.
- [3] S.V. Gnedenkov, et al., *Surf. Coat. Technol.* 145 (1–3) (2001) 146.
- [4] A.A. Voevodin, et al., *Surf. Coat. Technol.* 86–7 (1–3) (1996) 516.
- [5] J. Tian, et al., *Surf. Coat. Technol.* 154 (1) (2002) 1.
- [6] X. Nie, et al., *Surf. Coat. Technol.* 149 (2–3) (2002) 245.
- [7] L.R. Krishna, K.R.C. Somaraju, G. Sundararajan, *Surf. Coat. Technol.* 163–164 (2003) 484.
- [8] R. Barik, et al., *Tri-Service Corrosion Conference*, Navmar Applied Science Corp., Chester, PA, 2003, (November).
- [9] A.L. Yerokhin, et al., *Surf. Coat. Technol.* 130 (2–3) (2000) 195.
- [10] P.I. Butyagin, Y.V. Khokhryakov, A.I. Mamaev, *Mater. Lett.* 57 (2003) 1748.
- [11] S.V. Gnedenkov, et al., *Surf. Coat. Technol.* 123 (2000) 24.
- [12] A.L. Yerokhin, et al., *Surf. Coat. Technol.* 110 (3) (1998) 140.
- [13] A.L. Yerokhin, A. Leyland, A. Matthews, *Appl. Surf. Sci.* 200 (1–4) (2002) 172.
- [14] G. Sundararajan, L.R. Krishna, *Surf. Coat. Technol.* 167 (2003) 269.
- [15] Y. Guangliang, et al., *J. Alloys Compd.* 345 (2002) 196.
- [16] W.B. Xue, et al., *Surf. Coat. Technol.* 36 (2001) 2615.
- [17] W.B. Xue, et al., *Mater. Lett.* 52 (6) (2002) 435.
- [18] Y. Han, S.H. Hong, K.W. Xu, *Surf. Coat. Technol.* 168 (2–3) (2003) 249.
- [19] D.B. Wiles, R.A. Young, *J. Appl. Crystallogr.* 14 (1981) 149.
- [20] T.W. Clyne, *Key Eng. Mater.* 116/7 (1996) 307.
- [21] W.C. Oliver, G.M. Pharr, *J. Mater. Res.* 7 (6) (1992) 1564.
- [22] W.B. Xue, et al., *J. Am. Ceram. Soc.* 81 (5) (1998) 1365.